RESEARCH ARTICLE

Design and Development of a High-Gain Broadband Balanced Antipodal Vivaldi Antenna Using a 3D-Printed Shaped Dielectric Lens

SANGHAMITRO DAS[1], (Member, IEEE), **HELENA CLAVIN**[1,2],
KAUSHIK DEBBARMA[1], (Member, IEEE), **SATISH KUMAR SHARMA**[1], (Senior Member, IEEE),
PHILIP M. LAMBERT[3], AND **COLBY O. HOBART**[3]

[1]Department of Electrical and Computer Engineering, San Diego State University, San Diego, CA 92182, USA
[2]Galtronics USA Inc., Tempe, AZ 85284, USA
[3]Fortify Inc., Boston, MA 02129, USA

Corresponding author: Satish Kumar Sharma (ssharma@sdsu.edu)

ABSTRACT A broadband balanced antipodal Vivaldi antenna (BAVA) has been reported along with a novel 3D-printed shaped dielectric lens (SDL) for aiding in gain enhancement, largely towards the higher frequencies. The complete BAVA with SDL (BAVA-SDL) structure exhibits a broad simulated bandwidth of 3.8 GHz to over 60 GHz (>15.8:1). The 3D SDL enables an ever-increasing gain profile by compensating for the large phase errors that occur particularly at higher frequencies over a wide range of 45–60 GHz. The maximum simulated broadside gain reaches 24 dBi at 54 GHz. A Digital Light Processing (DLP) based 3D printing technique has been used to fabricate the SDL, where periodic unit lattice cells with air inclusions have been implemented for manipulating the corresponding relative permittivity. Measurements could be carried out until 45 GHz due to limitations from the fabrication process. Nevertheless, the measured results were found to be in very good agreement with their simulated counterparts.

INDEX TERMS Balanced antipodal Vivaldi antenna (BAVA), shaped dielectric lens (SDL), phase correction, 3D printing, high gain, broadband.

I. INTRODUCTION

Since its inception in 1979 [1], Vivaldi antennas have been used widely as an alternative of bulky ridged horn antennas, in a variety of applications including Ultrawideband (UWB), 5G new radio (5G-NR) and satellite communications, microwave imaging and radars particularly due to their very wide bandwidths, high gain, compact size, low sidelobe and cross-polarization levels, high front-to-back ratios, and easy planar integration with devices [2], [3], [4], [5], [6], [7], [8], [9]. The major limitation of the original coplanar Vivaldi antenna (CVA) design was that its impedance bandwidth was restricted by the frequency response of the balun structure (typically a microstrip-to-slotline transition) employed at

their feeds [10]. An equivalent structure, called the antipodal Vivaldi antennas (AVAs) [11], resolves this issue by employing a different balun structure (e.g., a microstrip-to-double-sided-parallel-stripline transition), which can exhibit extremely broad bandwidths [12]. However, since the conductive layers of an AVA are not on the same plane, it suffers from issues like beam squinting and high cross-polarization radiation, particularly at the higher frequencies. Balanced antipodal Vivaldi antennas (BAVAs) employ an additional conductive layer in order to reduce the cross-polarization radiation at higher frequencies, which also minimizes the beam squint [13].

Despite the very wide bandwidths, the radiation performance, e.g., gain, of an AVA or a BAVA can degrade as the frequency go high, mainly due to the larger amount of phase errors occurring at the aperture. Many approaches

exist in the literature for improving the Vivaldi gain. The simplest technique to enhance the performance of a Vivaldi antenna is perhaps to modify the shape of the conductive traces and/or apply periodic slots or corrugations at the edge of the radiating conductive traces [14], [15], [16], [17]. In addition to reducing the lower cut-off frequency of the Vivaldi antenna, this technique also allows to enhance gain and reduce sidelobes. Different slot/corrugation shapes have been studied, e.g., rectangular, triangular, sinusoidal etc., and maximum gain values up to 18.75 dBi could be achieved in [15]. However, the amount of gain enhancement using these techniques is rather small, and electrically large apertures are usually required in order to realize gain values as high as that reported in [15]. Another technique to enhance the Vivaldi antenna gain is to place a parasitic patch right in the middle of the aperture [18], [19], [20], [21]. The parasitic patch helps focus the fields towards the endfire direction by eliminating phase-reversals at the aperture edges, which typically results in higher sidelobes and off-axis radiations. The shape of the patch can be either elliptical, trapezoidal or diamond-shaped. A maximum measured gain of 16 dBi could be achieved in [19], where both elliptical parasitic patch and corrugations were employed.

The next technique involves dielectric lenses at the front of the Vivaldi antenna, which helps enhance the antenna gain and reduce sidelobes by minimizing the aperture phase error, such that the outgoing phase fronts are almost planar. There have been many examples of dielectric lenses in the literatures [22], [23], [24], [25], [26], [27], [28], [29], [30], and [31]. These lenses can either be 2D-planar (i.e., on the same plane as the dielectric substrate of the Vivaldi antenna) or 3D, and can have various shapes like elliptical [22], [23], circular [24], rectangular [25], diamond-shaped [26], rod-shaped [27], trapezoidal [28], [29], [30], and spherical-axicon [31]. The circular lens in [24] employed multiple dielectric layers of different relative permittivities in order to enhance gain. The 3D dielectric lens in [31] was applied to a polarization-reconfigurable orthogonally-placed CVA pair, where maximum gain value of 15.4 dBi could be realized. The highest gain value of 20.5 dBi was realized in [23] by surrounding the AVA and elliptical lens with another dielectric box made out of a different dielectric, which provided further correction to the aperture phase. The aperture phase correction can also be performed by placing metamaterials between the conductive traces of the antenna [32], [33], [34], [35]. Zero-index and near-zero-index metasurfaces have been employed in [32] and [33], respectively in order to realize gain values up to ∼14 dBi. In [34], the metamaterial phase correcting structure was accompanied by an elliptical parasitic patch, which helped producing a maximum gain of 14.4 dBi. In [35], the whole AVA structure was covered using metamaterial slabs to enclose all the fields around the AVA, such that phase correction is not limited to only the plane of the antenna. The maximum gain value obtained for this setup was 17.7 dBi. However, as it can be perceived, designing a metamaterial

phase correcting structure is more complex compared to an equivalent dielectric structure. Finally, the performance of a Vivaldi antenna can also be improved by means of computational optimization techniques like particle swarm optimization (PSO), genetic algorithm (GA), multi-objective PSO (MOPSO), multi-objective GA (MOGA) etc., which would allow one to find optimum trade-offs between two or more antenna parameters, e.g., dimension, bandwidth, gain, sidelobe level, cross-polarization etc. Some examples can be found in [36] and [37]. However, it is evident that the success of these kind of solutions depend solely on the training of the solver, which may require a large amount of time and other resources.

Most of the references discussed above employ a 2D lens, which performs phase correction on only one plane (E–plane), as a result of which the gain enhancement is not very high. The AVA reported in [23] was surrounded by a slab of dielectric, however it was not aimed towards correcting the phase errors on both the orthogonal E– and H–planes, as a result of which the gain enhancement is only 8 dB. Although the lens reported in [31] had a 3D shape, it did not encompass the entire antenna aperture as it was placed only in front of the aperture. Consequently, the gain enhancement was only ∼5–6 dB. The metamaterial slab design in [35] offered the highest gain enhancement of ∼13–14 dB (eye-estimated from the given plots), since the slabs enabled phase corrections on both the planes, while covering the aperture entirely. However as mentioned earlier, optimizing metamaterials through a proper unit cell design is generally a more complicated process.

In this work, a simple BAVA design has been presented in conjunction with a 3D shaped dielectric lens (SDL), and unlike most of the aforementioned examples, the 3D SDL encompasses the aperture fields on both E– and H–planes, thus enabling phase corrections on both the planes, and thereby allowing a larger gain enhancement (>16 dB) for the BAVA. Some preliminary simulated results were presented in [38], where a teardrop-shaped SDL was used. Later on, an attempt was made to fabricate the teardrop-shaped SDL using Teflon, which turned out to be quite challenging owing to its curved side profiles, and also the measurement results were found to be non-conclusive due to the lossy nature of Teflon at higher frequencies. However, in the presented work, the SDL has been optimized further for easier manufacturability. The SDL reported here comprises a simple hemispherical section for phase correction and a conical section with a straight side profile that are much easier to fabricate. The conical section helped equalize the phase response on both the orthogonal planes, while reducing the total amount of phase errors somewhat, and also allowed to secure the hemispherical structure at its designated place in front of the aperture. A 3D-printable low-loss dielectric material was used to fabricate the SDL, where a unique unit lattice cell with air inclusion was used to manipulate the relative permittivity, which also lowered the overall dielectric loss and lens weight. Another notable contribution of this manuscript is the inclusion of a generalized analytical
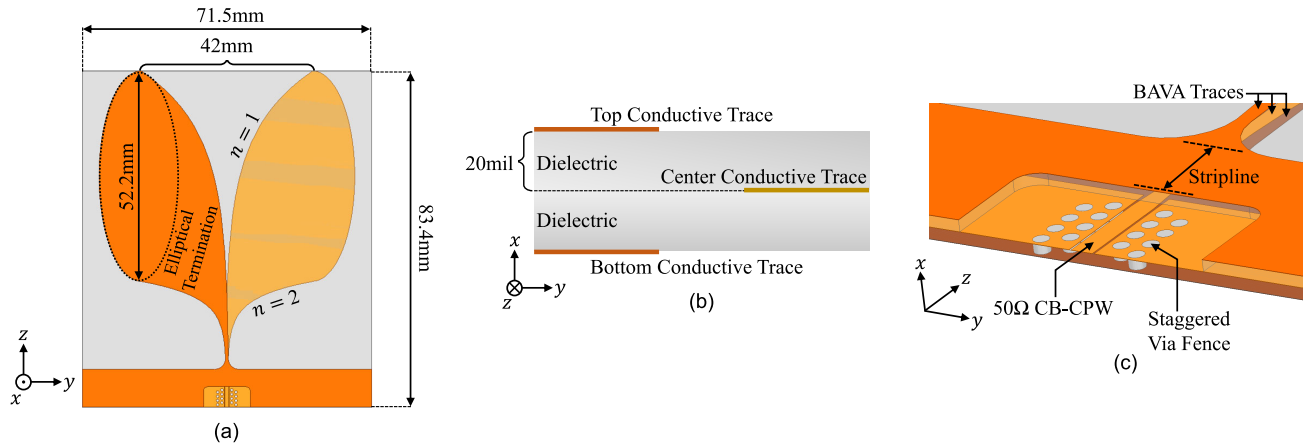
FIGURE 1. (a) Designed BAVA, (b) cross-section of BAVA, and (c) feed section.

background, which sheds light on the working principle of the presented SDL. Corresponding measurements were performed on the BAVA-SDL, and the measured results were found to be in good agreement with the simulated.

Section II describes the design of the BAVA along with the corresponding simulated results. Details of the SDL structure are provided in Section III, along with the analytical equations and corresponding working mechanism. The phase correction performance of the designed SDL was demonstrated in the same section, along with the enhanced BAVA performance. The fabrication of the SDL along with the corresponding 3D printing technology are discussed in Section IV. The measured results are also presented in the same section. Finally, the reported gain enhancement technique has been compared with some of the other reported techniques in Section V, following which the work is concluded in Section VI.

II. DESIGN OF THE BALANCED ANTIPODAL VIVALDI ANTENNA

Two 20-mil-thick Rogers RT/duroid® 5880 dielectric substrates ($\varepsilon_r = 2.2$, $\tan\delta = 0.0009$) were considered for the BAVA design. The three conducting traces of the BAVA were arranged on both sides of the two dielectric layers. Moreover, each of these three traces were assigned a thickness of 17 μm (1/2 -oz thick copper cladding) to model the practical losses of the bulk copper. A schematic diagram of the BAVA is shown in Fig. 1(a), along with a cross-section of the corresponding dielectric and conducting layers in Fig. 1(b). As it can be seen, the aperture comprises two exponentially-tapered profiles: $n = 1$ and 2, which indicate the inside and outside profiles, respectively. The tapering profiles were created using the following equation:

$$y(z) = ae^{p_n(z-z_0)} - y_0 \tag{1}$$

where, $a = 0.175$ mm, $p_1 = 67.5$ ($n = 1$ for inside profile), $p_2 = 250$ ($n = 2$ for outside profile), $z_0 = 12$ mm, and $y_0 = 0.34$ mm. Elliptical terminations with major and minor

radii of 26.1 mm and 10.44 mm, respectively, were used at the end of each of the BAVA traces in order to enable a smooth transition of the fields from the aperture to the free space by eliminating undesired diffractions from the aperture ends. As shown in Fig. 1(c), the feed section of the BAVA comprises a conductor-backed coplanar waveguide (CB-CPW) section, followed by a stripline section that eventually transitions into the three BAVA traces. For the CB-CPW section, a cut out has been created on the top dielectric layer, which enables easy integration of an external coaxial connector. Also, staggered via fence has been applied on both sides of the CB-CPW line in order to suppress unwanted substrate modes. Simulations were performed using Ansys HFSS.
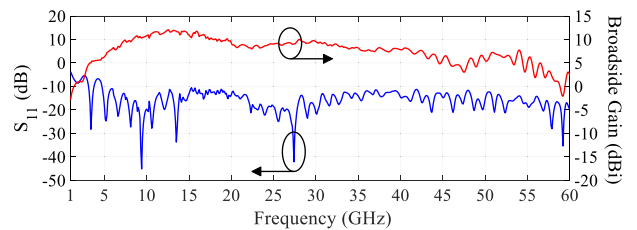

FIGURE 2. Simulated S_{11} and gain vs. frequency of the designed BAVA.

The simulated S_{11} and gain vs. frequency characteristics of the BAVA are shown in Fig. 2. The BAVA has an impedance bandwidth spanning from 4.7 GHz to over 60 GHz (>12.8:1). Simulations were not performed beyond 60 GHz as the structure became electrically very large, which lead to very high memory requirements and simulation times. The broadside gain of the BAVA increases initially until 12.6 GHz, where the corresponding gain value is 12.06 dBi. However, following 12.6 GHz, the phase errors occurring at the antenna aperture started to become significant, which led to a drop in the broadside gain value. The gain drop becomes even more significant at higher frequencies, e.g., beyond 40 GHz where the gain value drops below 8 dBi. The SDL structure described in Section III aims to improve the

gain by compensating the phase errors particularly at these higher frequency ranges.

III. DESIGN OF THE SHAPED DIELECTRIC LENS

A. CONSTRUCTION AND WORKING PRINCIPLE

A typical phase correcting structure transforms non-planar phase fronts into planar ones, which in turn enhances overall directivity of an antenna system [39], [40]. In this work, a hemispherical phase correcting structure of radius R (i.e., thickness at $x = y = 0$ planes) has been considered to enhance the BAVA gain – particularly in the higher frequencies – over a wide range of 45–60 GHz, where the broadside gain had degraded the most due to large phase errors. The complete SDL structure comprises the hemispherical section along with a conical section added to the bottom, as shown in Fig. 3. The conical section serves two main purposes:
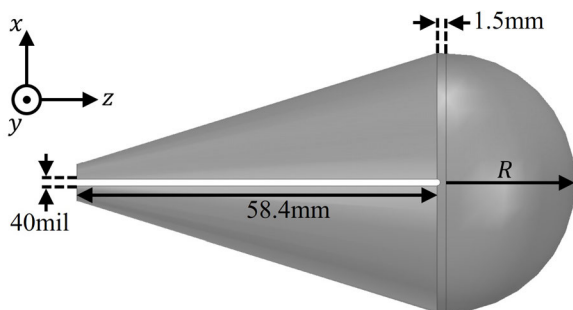

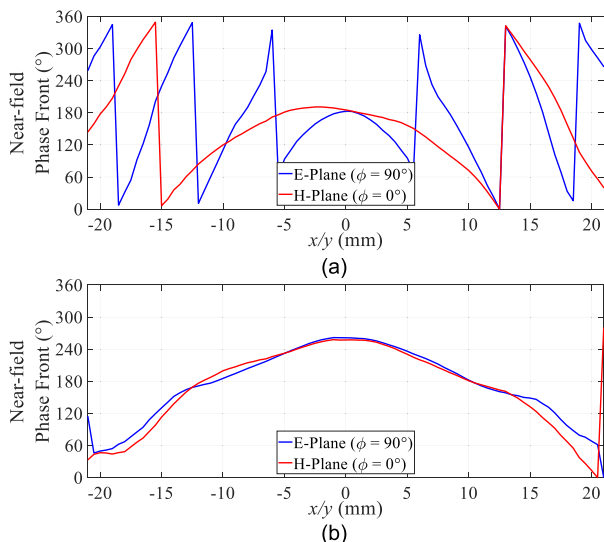**FIGURE 3.** SDL structure with hemispherical and conical sections.

FIGURE 4. Effect of conical section of the SDL on the simulated near-field phase fronts at 45 GHz: (a) without and (b) with the conical section.

1) Since the BAVA is a planar structure, the near-field phase fronts on E– (yz plane, or $\phi = 90°$) and H– (xz plane, or $\phi = 0°$) planes are non-identical. The 3D conical shape enables the phase fronts to be almost identical on both planes, with relatively less amount of
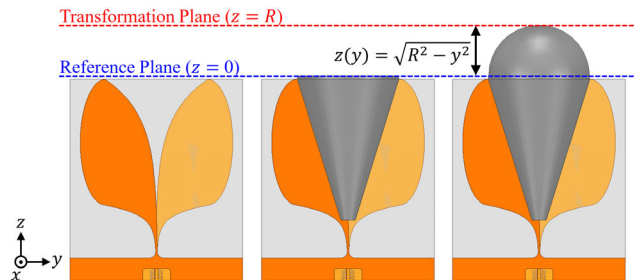

FIGURE 5. Reference and phase transformation planes for the BAVA without SDL, with only the conical section, and with the full SDL structure.

total phase error (can be determined from the number of phase wrappings). An example is shown in Fig. 4. Consequently, the transformed phase fronts following the 3D hemispherical structure become almost planar on both the planes, unlike the 2D cases described in Section I, which in turn helps realizing higher amount of gain.

2) The conical section also helps holding the hemispherical structure at its designated place in front of the aperture by the help of a slit (of width equal to the total BAVA thickness) that runs down the length of the conical section.

The BAVA without any phase correcting structure, with only the conical section, and with the full SDL structure are shown in Fig. 5. The reference plane ($z = 0$), where the near-field phase fronts were studied, is considered just outside the BAVA aperture at a distance of 1.5 mm. The phase compensation in the z–direction offered by the hemispherical section can be given as [41]:

$$\phi\left(\varepsilon_r, z\right) = \angle\left[\cos\left(k_z z\right) + j\sin\left(k_z z\right)\left(\frac{1 + \varepsilon_r}{2\sqrt{\varepsilon_r}}\right)\right] - k_0 z \quad (2)$$

where,

$$z(x) = \sqrt{R^2 - x^2}, z(y) = \sqrt{R^2 - y^2} \text{ and } k_z = k_0\sqrt{\varepsilon_r} \quad (3)$$

In the above equations, $z(x)$ and $z(y)$ are the hemispherical thickness profiles of the phase correcting structure in x– and y–directions, respectively, ε_r is the relative permittivity of the SDL material, and k_0 is the free-space wavenumber. In order to demonstrate the phase compensation mechanism using a semi-analytical approach using the proposed hemispherical SDL section, first the near-field phase front for the BAVA with the conical section would be obtained from the simulations at the aforementioned reference plane. Next, the amount of phase compensation were computed using (2). Finally, the transformed (i.e., compensated) phase fronts at the output of the hemispherical section (transformation plane, i.e., at $z = R$) could be computed by simply combining the simulated near-field phase front values and the phase compensation introduced by the hemispherical section.

B. PARAMETRIC STUDIES ON ε_r AND R

In order to determine the best choices for the relative permittivity (ε_r) of the SDL, and the dimension of the hemispherical section that would enable maximum gain enhancement in 45–60 GHz range, two independent studies were conducted. In the first study, ε_r of the SDL was varied while keeping the radius of the hemispherical section R unchanged. The value of R was initially considered to be 21 mm, which precisely encompasses the aperture opening of the BAVA. The near-field phase front and the corresponding gain values were studied for three ε_r values: 2.1, 3.9 and 6. Moreover, for each of these cases, the dielectric loss parameter (tanδ) was maintained at 0.001 in order to ensure a fair comparison. The corresponding gain vs. frequency along with the computed near-field phase fronts at 45 GHz and 60 GHz are shown in Fig. 6. Near-field phase fronts are only shown on the E-plane for brevity. It can be clearly observed that the phase fronts corresponding to $\varepsilon_r = 2.1$ are much flatter than those obtained for the other ε_r values, resulting in most amount of gain enhancement in the desired frequency range. This occurs as the aperture fields experience a smooth transition while progressing into the conical section of the SDL structure from the BAVA dielectric substrate that has an almost equal relative permittivity.
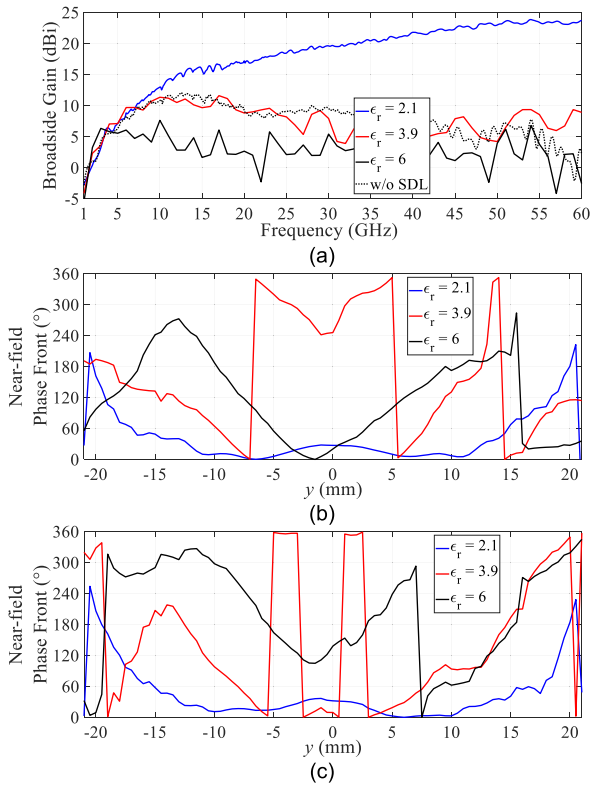

FIGURE 6. (a) Simulated broadside gain vs. frequency for different ε_r of the SDL, corresponding E-plane near-field phase fronts at (b) 45 GHz and (c) 60 GHz.

In the second study, radius of the hemispherical section R was varied while keeping the ε_r fixed at 2.1. Three values of R were considered for this study: 21 mm, 25 mm and
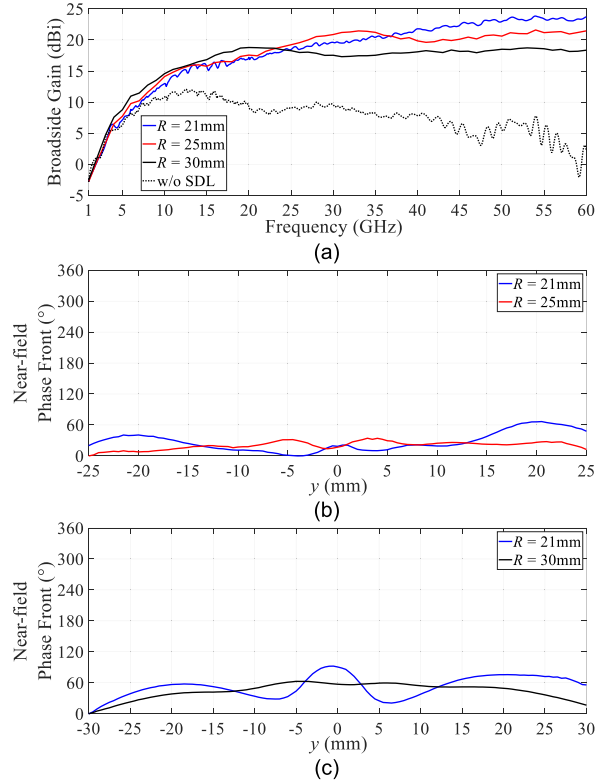

FIGURE 7. (a) Simulated broadside gain vs. frequency for different R of the SDL, corresponding E-plane near-field phase fronts at (b) 33 GHz and (c) 20 GHz.

30 mm. The corresponding gain vs. frequency plot is shown in Fig. 7(a). As it can be seen, $R = 21$ mm case enables maximum gain values in the desired frequency range of 45–60 GHz, and the maximum-gain region slowly shifts towards lower frequencies with increasing R. Maximum gain values of 21.5 dBi at 33 GHz and 18.8 dBi at 20 GHz could be attained for $R = 25$ mm and 30 mm, respectively. This is consistent, since a larger hemispherical radius would be required at lower frequencies in order to enable proportionate phase compensation. It should also be noted from Fig. 7(a) that if the maximum gain enhancement with respect to the without-SDL case is considered for the entire frequency range, it occurs at frequencies beyond 45 GHz, where the corresponding without-SDL gain has dropped drastically. However, if the amount of gain enhancement is considered only at a particular frequency (e.g., either at 20 GHz or at 33 GHz), the corresponding R value has the best gain enhancement performance. The gain values are ∼1.6 dB more for both $R = 25$ mm and 30 mm cases at their respective maximum-gain frequencies, compared to the same for $R = 21$ mm. A comparison of near-field phase fronts for $R = 21$ mm and 25 mm at 33 GHz, and 21 mm and 30 mm at 20 GHz are shown in Figs. 7(b) and 7(c), respectively. It can be easily seen that although mostly flat, $R = 25$ mm and $R = 30$ mm in Figs. 7(b) and 7(c), respectively, have cumulatively lower phase error than the $R = 21$ mm case (∼30° less), thus implying slightly higher gain at respective

frequencies. In conclusion, it can be easily seen from the above studies that $\varepsilon_r = 2.1$ and $R = 21$ mm cases result in the best gain values in the range of 45–60 GHz range, while enabling the maximum gain enhancement.
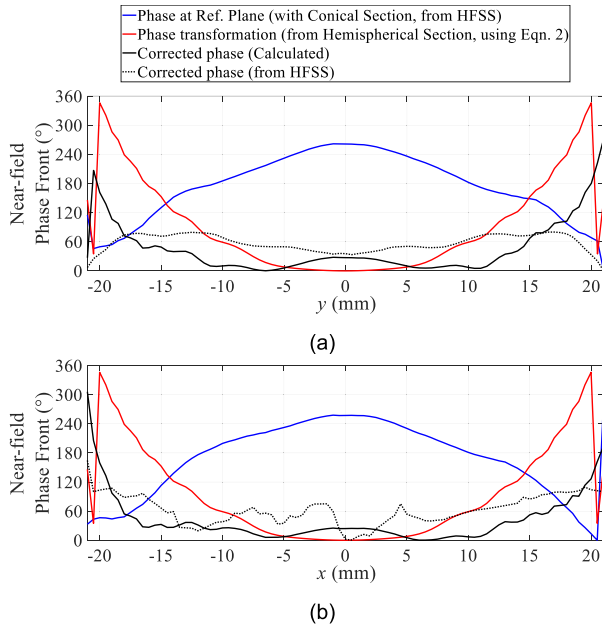

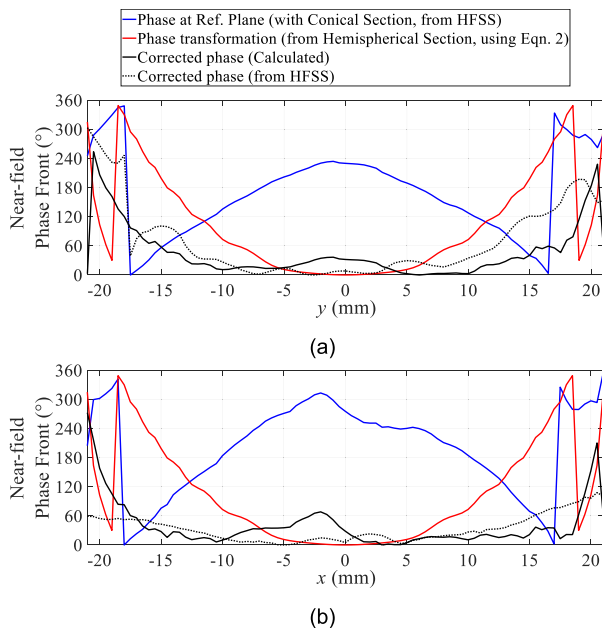**FIGURE 8.** Phase transformation using hemispherical section of the SDL at 45 GHz: (a) E–plane, and (b) H–plane.

FIGURE 9. Phase transformation using hemispherical section of the SDL at 60 GHz: (a) E–plane, and (b) H–plane.

C. FINAL DESIGN AND SIMULATION STUDIES

The BAVA was simulated in HFSS along with the complete SDL structure with $\varepsilon_r = 2.1$ and $R = 21$ mm. All the different phase fronts at 45 GHz and 60 GHz are shown in Figs. 8 and 9,
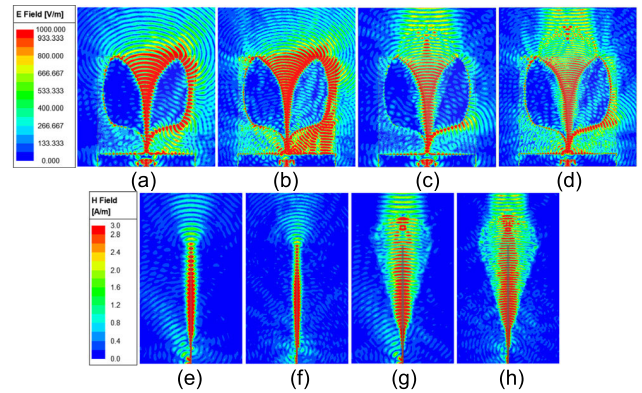

FIGURE 10. Simulated near-field phase fronts: (a) E–plane, 45 GHz, without SDL, (b) E–plane, 60 GHz, without SDL, (c) E–plane, 45 GHz, with SDL, (d) E–plane, 60 GHz, with SDL, (e) H–plane, 45 GHz, without SDL, (f) H–plane, 60 GHz, without SDL, (g) H–plane, 45 GHz, with SDL, (h) H–plane, 60 GHz, with SDL.

respectively, along with the simulated corrected phase fronts obtained directly from HFSS in presence of the complete SDL structure. As it can be seen, the corrected phase fronts – both computed and simulated – are much flatter, i.e., with less phase error, when compared to the uncorrected phase fronts for both semi-analytical and simulated cases. This, as shown in Section III-B, resulted in very high gain values in the target frequency range of 45–60 GHz. The simulated field surface plots at both E– and H–planes for 45 GHz and 60 GHz are shown in Fig. 10, which once again confirm the flatness of the outgoing phase fronts. The simulated S_{11} along with the gain vs. frequency in presence of the SDL are shown in Fig. 11(a). The onset frequency of the -10-dB S_{11} improves by ~19%, resulting in an impedance bandwidth spanning from 3.8 GHz to over 60 GHz ($> 15.8:1$). The broadside gain at the lower end of the bandwidth, i.e., at 3.8 GHz is ~6 dBi, and reaches ~24 dBi around 54 GHz, with an enhancement of > 16 dB in the 45–60 GHz range. The maximum gain enhancement of 25.4 dB was obtained at 59.2 GHz. The simulated radiation and total efficiencies for the BAVA-SDL are better than 86% and 83%, respectively, in the entire frequency range. The corresponding co-to-cross polarization separation and front-to-back ratio are shown in Fig. 11(b). It can be seen that throughout the bandwidth, the BAVA with SDL maintains a co-to-cross polarization separation of > 16.4 dB with an average > 20 dB, and a front-to-back ratio of > 10 dB with maximum value of 48.7 dB. The aperture efficiency was found to be between 40%–50% in the range of 40–55 GHz, and between 30%–40% in the range beyond 55 GHz.

Group delay is an important metric to quantify the dispersion of a broadband antenna, particularly in the context of pulse transmission. The group delay for the BAVA-SDL was extracted from a time-domain simulation performed in the CST Microwave Studio, and is shown in Fig. 12. It can be seen that at the lower end of the band, the fluctuations in the group delay is ~1 ns, which later reduces to ~0.5 ns
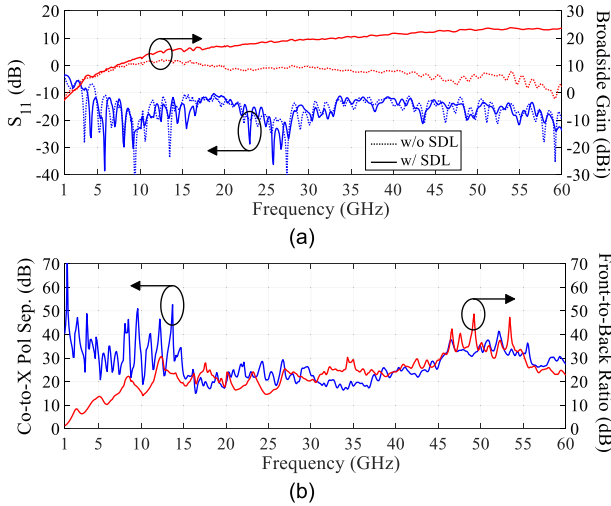
FIGURE 11. Simulated (a) S_{11} and gain vs. frequency of the BAVA with and without SDL, (b) corresponding co-to-cross-pol separation and front-to-back ratio.
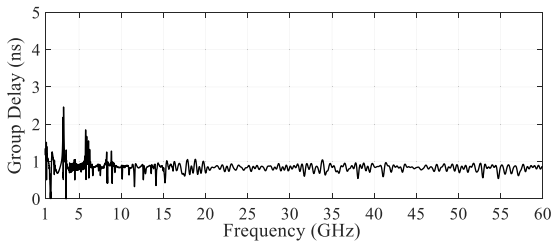

FIGURE 12. Simulated group delay for the BAVA-SDL.

for most of the band, indicating even lower dispersion. This implies that if a short pulse is radiated through the antenna, the resulting ringing at the end of the radiated pulse will be minimal, which is critical for applications like microwave imaging and ground penetrating radars (GPRs). Moreover, the group delay is comparable with that reported in [19], where the bandwidth of operation is in the same order.

IV. FABRICATION AND MEASUREMENT

The BAVA was fabricated at the San Diego State University using a LPKF ProtoMat S63 milling machine. The SDL was printed at the Fortify, Inc. facility using their FLUX Core 3D printer. The material used for the SDL is Radix^{TM} photocurable dielectric material ($\varepsilon_r = 2.8$, $\tan \delta = 0.0043$ at 10 GHz and 0.0046 at 24 GHz) from Rogers Corporation. The printer uses a process called Digital Light Processing (DLP), where a UV LED projector shines images of the cross-sectional layers (that were created in the 3D printing software after slicing the whole structure) using UV light into a vat of liquid photocurable resin, i.e., Radix^{TM}. The projected image changes for each layer, curing and stacking solid layers of the dielectric photopolymer on top of one another. The structure is built in this layer-by-layer fashion until the complete part has been fabricated. The part is then removed from the printer,

cleaned of residual liquid resin and support structure material, and post-cured in thermal and UV ovens. It can be recalled that the ε_r of the SDL material described in Section III was selected to be 2.1 in order to have a good transition of fields from the antenna substrate to the lens. Nevertheless, with the aforementioned 3D printer and the Radix^{TM} material, it is possible to print complex 3D structures such as lattices with air gaps in order to create an effective media that has a ε_r lower than 2.8. The lattice shape used in this case is a gyroid, which is a type of Triply Periodic Minimal Surface (TPMS). The relationship between the air volume fraction and the effective relative permittivity is determined using a Reverse Claussius-Mossotti model [42]:

$$\varepsilon_{r,eff} = \varepsilon_{r,resin} \cdot \frac{1 + 2v_{air}\left(\frac{1-\varepsilon_{r,resin}}{1+2\varepsilon_{r,resin}}\right)}{1 - v_{air}\left(\frac{1-\varepsilon_{r,resin}}{1+2\varepsilon_{r,resin}}\right)} \quad (4)$$

where, $\varepsilon_{r,eff}$ is the effective permittivity of the gyroid lattice region, v_{air} is the volume fraction of air, and $\varepsilon_{r,resin}$ is the permittivity of the solid dielectric material used to form the lattice. For a lattice geometry to behave as an effective medium, the features of the lattice need to be sufficiently sub-wavelength. In this design, the maximum desired operational frequency is 60 GHz, with an associated wavelength of 5 mm. The minimum lattice dimension that could be successfully fabricated following the manufacturing tolerances is 4 mm, where the pores are of 0.45 mm in diameter, and the walls are 1 mm in thickness. With these dimensions, the 4 mm lattice yields an air fraction of 33.3%, resulting in $\varepsilon_{r,eff} = 2.1$. Additionally, the inclusion of air-gaps would also reduce the losses ($\tan \delta$), and make the entire structure lightweight. The fabrication model of the SDL along with the lattice are shown in Fig. 13(a), and the fabricated SDL is shown in Fig. 13(b) along with the BAVA. The fabricated SDL weighed only 50.73 gm, as compared to 112.24 gm, had it been fabricated using solid Teflon ($\varepsilon_r = 2.1$).

The S_{11} and radiation pattern measurements were carried out at the Antenna and Microwave Laboratory (AML), San Diego State University (SDSU). The S_{11} was measured using a Keysight N5225A PNA, which has a maximum range of 50 GHz. The measured S_{11} along with its simulated counterpart is shown in Fig. 14. It can be seen that the measured −10-dB bandwidth also starts from the same 3.8 GHz as the simulated and spans beyond 50 GHz. The setup for measuring the radiation patterns inside the far-field anechoic chamber at AML, SDSU is shown in Fig. 15. In order to hold the BAVA-SDL at its designated place, a 3D-printed mount has been created, which also prevented the bending of the BAVA layers due to the weight of the SDL. Normalized measured co–polarization radiation patterns along with their simulated counterparts for both with and without the SDL are shown in Fig. 16, at a few frequencies spanned evenly throughout the bandwidth. The normalization was performed with respect to the broadside maxima of the corresponding BAVA-SDL co-polarization radiation pattern. It can be seen that the measured patterns
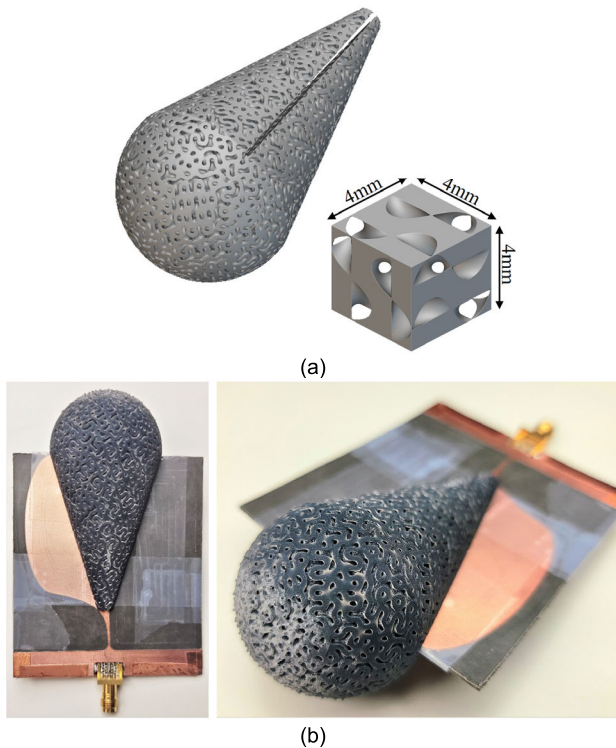
FIGURE 13. (a) Fabrication model of SDL with gyroid unit cell, (b) fabricated BAVA-SDL.
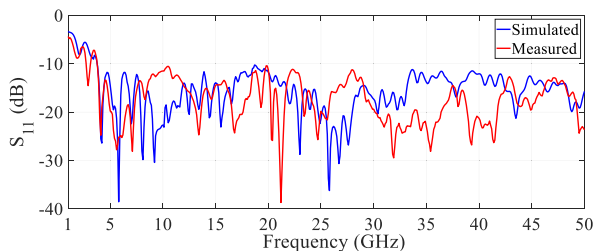

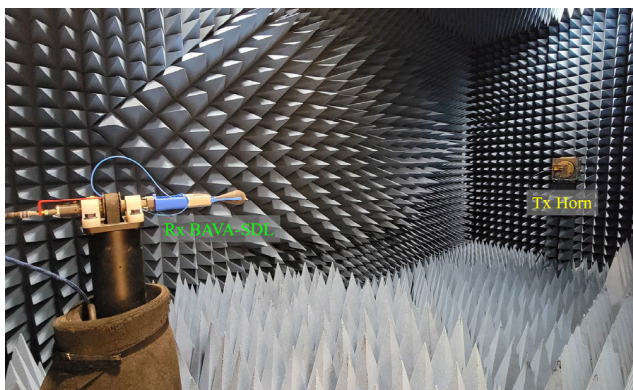**FIGURE 14.** Simulated and measured S$_{11}$ for the BAVA-SDL.

FIGURE 15. Measurement setup inside the far-field anechoic chamber at the AML, SDSU.

agree very well with the simulated, with approximately similar half-power beamwidths (HPBWs), which is essentially a manifestation of almost equal simulated and measured

directivities. The simulated vs. measured broadside gain improvement and co-to-cross polarization separations are shown in Fig. 17. It can be observed that for both the cases, the measured data are comparable to that from simulation. Nevertheless, it should be noted that meaningful radiation patterns could only be obtained until 45 GHz, which is potentially due to the finite lattice size of the SDL that became comparable to the wavelength at frequencies beyond 45 GHz, and also due to some increased losses in the dielectrics used.

V. COMAPARISON WITH OTHER GAIN ENHANCEMENT TECHNIQUES

The performances of the BAVA-SDL were compared with a few other examples employing different gain enhancement techniques. Before starting the comparison, the following factors should be noted:

1) The reported works do not always mention the onset frequency of –10-dB S$_{11}$ response, which makes an accurate comparison of the antenna bandwidth difficult.
2) The initial aperture dimensions for the reported designs are not always the same. Moreover, the aperture sizes of some of these antennas were often miniaturized before the application of a gain-enhancing structure, either by employing slots and corrugations at the antenna edges, or by employing dielectric substrates with higher ε_r. This automatically changes the initial gain value that needs to be enhanced. Consequently, it is somewhat unfair to compare the final gain values of these antennas with the reported one, since a lot of conditions are not identical.
3) In most of these works, only the final maximum gain values are reported, which makes estimation of the exact amount of gain enhancement somewhat inaccurate, and they had to be eye-estimated from the plots given in the papers. Nevertheless, it is a much more independent metric to compare the different gain enhancement techniques, compared to the antenna bandwidth or maximum broadside gain.

In the comparison presented in Table 1, the antenna dimensions, bandwidth, maximum broadside gain, and the amount of gain enhancement were included along with the corresponding gain enhancement technique. As it can be seen, despite having a relatively smaller aperture size than most of the other examples, the reported BAVA-SDL demonstrates the maximum amount of gain enhancement, along with the maximum broadside gain value. It should also be noticed that in order to achieve large gain enhancements, the antenna with lens can no longer be just planar. Rather, the lens needs to have a 3D shape in order to facilitate phase corrections on both E- and H-planes. However, the profile size of the lens on the H-plane can be reduced by employing a gradient refractive index (GRIN) based design, which we plan to study in the future.
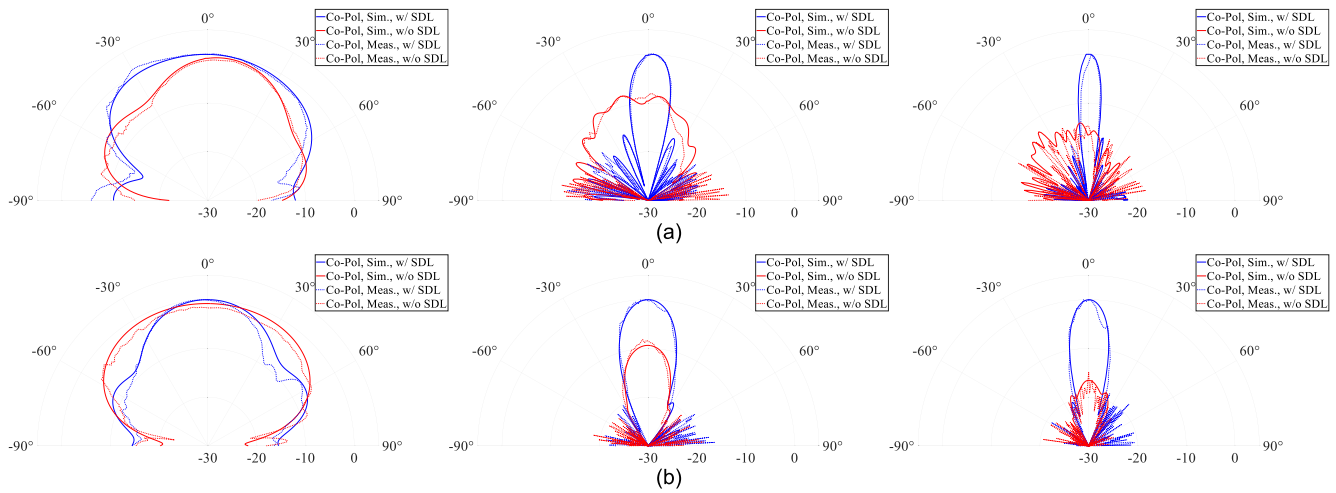
FIGURE 16. Simulated and measured co-polarization radiation patterns of the BAVA with and without SDL, at 5 GHz (*left*), 25 GHz (*center*) and 45 GHz (*right*): (a) E–plane and (b) H–plane.

TABLE 1. Comparison of different gain enhancement techniques employed on vivaldi antennas.

Ref.	Dimension	−10-dB S_{11} Bandwidth	Maximum Broadside Gain	Maximum Gain Enhancement	Technique Applied
[19]	$1.6\lambda_L \times 0.64\lambda_L \times 0.004\lambda_L$	2.5–57 GHz (22.8:1)†	16 dBi	3–4 dB up to 20 GHz	Parasitic patch/pseudoelement at the aperture
[23]	$1.8\lambda_L \times 0.53\lambda_L \times 0.11\lambda_L$	5–50 GHz (10:1)	20.5 dBi	8 dB	2D dielectric lens + Surrounded by dielectric box
[31]	$0.65\lambda_L \times 0.48\lambda_L \times 0.48\lambda_L$	0.65–6 GHz (9.2:1)	15.4 dBi	~7 dB*	3D dielectric lens
[34]	$1.3\lambda_L \times 0.6\lambda_L \times 0.004\lambda_L$	1–28 GHz (28:1)	14.6 dBi	~3–4 dB*	Parasitic patch/pseudoelement + Metamaterials
[35]	$0.74\lambda_L \times 0.5\lambda_L \times 0.1\lambda_L$	3.68–43.5 GHz (11.8:1)	17.7 dBi	~13–14 dB*	Metamaterial slabs
Proposed	$1.06\lambda_L \times 0.9\lambda_L \times 0.26\lambda_L$	3.8– >60 GHz (>15.8:1)	24 dBi	25.4 dB	3D shaped dielectric lens

† VSWR < 3, S_{11} < −6 dB
* Estimated from plot.
‡ λ_L is the wavelength at the lower end of the reported bandwidth.
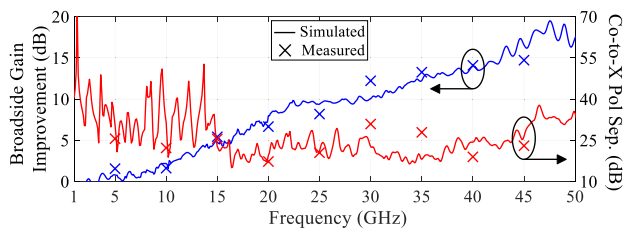

FIGURE 17. Simulated vs. measured broadside gain improvement and co-to-cross polarization separation for the BAVA-SDL.

VI. CONCLUSION

A novel 3D-printed shaped dielectric lens have been designed for compensating the phase errors of a BAVA antenna in order to significantly improve its pattern and gain at higher frequencies, while not affecting its impedance matching behavior. The SDL was designed to compensate for the large phase errors occurring at the BAVA aperture at higher frequencies, particularly in the range of 45–60 GHz. The final

BAVA-SDL exhibited a very broad simulated bandwidth of 3.8 GHz to over 60 GHz and the highest simulated gain value that was achieved is 24 dBi at 54 GHz. It should be noted that the designed SDL had a minimal effect on the impedance bandwidth and the low-frequency gain characteristics of the BAVA. The measured results agreed very well with the simulated, but the radiation performance was somewhat restricted by the finite lattice dimensions that could be realized during the 3D printing of the SDL. A smaller lattice dimension would enable gain enhancements at even higher frequencies. Finally, the SDL design can be easily optimized following the equations presented in Section III in order to enhance gain at other frequency ranges as well. Moreover, since the SDL is easily removable, it is possible to switch among multiple SDLs for different frequency ranges for the same BAVA design. Due to its very broad bandwidth and high gain, the BAVA-SDL can be used in various applications such as satellite communications, microwave imaging, 5G-NR base stations and electronic warfare systems.

REFERENCES

[1] P. J. Gibson, "The Vivaldi aerial," in *Proc. 9th Eur. Microw. Conf.*, Brighton, U.K., Sep. 1979, pp. 101–105.

[2] A. S. Dixit and S. Kumar, "A survey of performance enhancement techniques of antipodal Vivaldi antenna," *IEEE Access*, vol. 8, pp. 45774–45796, 2020.

[3] A. Zachary Hood, T. Karacolak, and E. Topsakal, "A small antipodal Vivaldi antenna for ultrawide-band applications," *IEEE Antennas Wireless Propag. Lett.*, vol. 7, pp. 656–660, 2008.

[4] S. Kumar, A. S. Dixit, R. R. Malekar, H. D. Raut, and L. K. Shevada, "Fifth generation antennas: A comprehensive review of design and performance enhancement techniques," *IEEE Access*, vol. 8, pp. 163568–163593, 2020.

[5] E. W. Reid, L. Ortiz-Balbuena, A. Ghadiri, and K. Moez, "A 324-element Vivaldi antenna array for radio astronomy instrumentation," *IEEE Trans. Instrum. Meas.*, vol. 61, no. 1, pp. 241–250, Jan. 2012.

[6] M. Abbak, M. N. Akinci, M. Çayören, and I. Akduman, "Experimental microwave imaging with a novel corrugated Vivaldi antenna," *IEEE Trans. Antennas Propag.*, vol. 65, no. 6, pp. 3302–3307, Jun. 2017.

[7] M. Moosazadeh, S. Kharkovsky, J. T. Case, and B. Samali, "Improved radiation characteristics of small antipodal Vivaldi antenna for microwave and millimeter-wave imaging applications," *IEEE Antennas Wireless Propag. Lett.*, vol. 16, pp. 1961–1964, 2017.

[8] F. Guangyou, "New design of the antipodal Vivaldi antenna for a GPR system," *Microw. Opt. Technol. Lett.*, vol. 44, no. 2, pp. 136–139, 2004.

[9] J. Guo, J. Tong, Q. Zhao, J. Jiao, J. Huo, and C. Ma, "An ultrawide band antipodal Vivaldi antenna for airborne GPR application," *IEEE Geosci. Remote Sens. Lett.*, vol. 16, no. 10, pp. 1560–1564, Oct. 2019.

[10] R. Natarajan, J. V. George, M. Kanagasabai, L. Lawrance, B. Moorthy, D. B. Rajendran, and M. G. N. Alsath, "Modified antipodal Vivaldi antenna for ultra-wideband communications," *IET Microw., Antennas Propag.*, vol. 10, no. 4, pp. 401–405, Mar. 2016.

[11] E. Gazit, "Improved design of the Vivaldi antenna," *IEE Proc. H (Microw., Antennas Propag.)*, vol. 135, no. 2, pp. 89–92, Apr. 1988.

[12] S.-G. Kim and K. Chang, "Ultrawide-band transitions and new microwave components using double-sided parallel-strip lines," *IEEE Trans. Microw. Theory Techn.*, vol. 52, no. 9, pp. 2148–2152, Sep. 2004.

[13] J. D. S. Langley, P. S. Hall, and P. Newham, "Novel ultrawide-bandwidth Vivaldi antenna with low crosspolarisation," *Electron. Lett.*, vol. 29, pp. 2004–2005, Nov. 1993.

[14] J. Bai, S. Shi, and D. W. Prather, "Modified compact antipodal Vivaldi antenna for 4–50-GHz UWB application," *IEEE Trans. Microw. Theory Techn.*, vol. 59, no. 4, pp. 1051–1057, Apr. 2011.

[15] Z. Briqech, A. Sebak, and T. A. Denidni, "High gain 60 GHz antipodal Fermi tapered slot antenna with sine corrugation," *Microw. Opt. Technol. Lett.*, vol. 57, no. 1, pp. 6–9, Nov. 2014.

[16] K. D. Phalak, Z. Briqech, and A. Sebak, "Ka-band antipodal fermi-linear tapered slot antenna with a knife edge corrugation," *Microw. Opt. Technol. Lett.*, vol. 57, no. 2, pp. 485–489, Dec. 2014.

[17] M. Moosazadeh, S. Kharkovsky, J. T. Case, and B. Samali, "UWB antipodal Vivaldi antenna for microwave imaging of construction materials and structures," *Microw. Opt. Technol. Lett.*, vol. 59, no. 6, pp. 1259–1264, Mar. 2017.

[18] I. T. Nassar and T. M. Weller, "A novel method for improving antipodal Vivaldi antenna performance," *IEEE Trans. Antennas Propag.*, vol. 63, no. 7, pp. 3321–3324, Jul. 2015.

[19] J. Eichenberger, E. Yetisir, and N. Ghalichechian, "High-gain antipodal Vivaldi antenna with pseudoelement and notched tapered slot operating at (2.5 to 57) GHz," *IEEE Trans. Antennas Propag.*, vol. 67, no. 7, pp. 4357–4366, Jul. 2019.

[20] J. Bang, J. Lee, and J. Choi, "Design of a wideband antipodal Vivaldi antenna with an asymmetric parasitic patch," *J. Electromagn. Eng. Sci.*, vol. 18, no. 1, pp. 29–34, Jan. 2018.

[21] Z. Li, X. Kang, J. Su, Q. Guo, Y. Yang, and J. Wang, "A wideband end-fire conformal Vivaldi antenna array mounted on a dielectric cone," *Int. J. Antennas Propag.*, vol. 2016, Aug. 2016, Art. no. 9812642.

[22] A. Molaei, M. Kaboli, S. A. Mirtaheri, and M. S. Abrishamian, "Dielectric lens balanced antipodal Vivaldi antenna with low cross-polarisation for ultra-wideband applications," *IET Microw., Antennas Propag.*, vol. 8, no. 14, pp. 1137–1142, Nov. 2014.

[23] M. Moosazadeh, "High-gain antipodal Vivaldi antenna surrounded by dielectric for wideband applications," *IEEE Trans. Antennas Propag.*, vol. 66, no. 8, pp. 4349–4352, Aug. 2018.

[24] D. Huang, H. Yang, Y. Wu, F. Zhao, and X. Liu, "A high-gain antipodal Vivaldi antenna with multi-layer planar dielectric lens," *J. Electromagn. Waves Appl.*, vol. 32, no. 4, pp. 403–412, Oct. 2017.

[25] N. Ghassemi and K. Wu, "Planar high-gain dielectric-loaded antipodal linearly tapered slot antenna for E- and W-band gigabyte point-to-point wireless services," *IEEE Trans. Antennas Propag.*, vol. 61, no. 4, pp. 1747–1755, Apr. 2013.

[26] J. Bourqui, M. Okoniewski, and E. C. Fear, "Balanced antipodal Vivaldi antenna with dielectric director for near-field microwave imaging," *IEEE Trans. Antennas Propag.*, vol. 58, no. 7, pp. 2318–2326, Jul. 2010.

[27] R. Kazemi, A. E. Fathy, and R. A. Sadeghzadeh, "Dielectric rod antenna array with substrate integrated waveguide planar feed network for wideband applications," *IEEE Trans. Antennas Propag.*, vol. 60, no. 3, pp. 1312–1319, Mar. 2012.

[28] M. Moosazadeh and S. Kharkovsky, "A compact high-gain and front-to-back ratio elliptically tapered antipodal Vivaldi antenna with trapezoid-shaped dielectric lens," *IEEE Antennas Wireless Propag. Lett.*, vol. 15, pp. 552–555, 2016.

[29] X. Li, Y. Xu, H. Wang, Y. Zhang, and G. Lv, "Low cross-polarization antipodal tapered slot antenna with gain bandwidth enhancement for UWB application," *J. Comput. Electron.*, vol. 17, no. 1, pp. 442–451, Oct. 2017.

[30] F. Wan, J. Chen, and B. Li, "A novel ultra-wideband antipodal Vivaldi antenna with trapezoidal dielectric substrate," *Microw. Opt. Technol. Lett.*, vol. 60, no. 2, pp. 449–455, Jan. 2018.

[31] R. Cicchetti, V. Cicchetti, A. Faraone, L. Foged, and O. Testa, "A compact high-gain wideband lens Vivaldi antenna for wireless communications and through-the-wall imaging," *IEEE Trans. Antennas Propag.*, vol. 69, no. 6, pp. 3177–3192, Jun. 2021.

[32] B. Zhou and T. J. Cui, "Directivity enhancement to Vivaldi antennas using compactly anisotropic zero-index metamaterials," *IEEE Antennas Wireless Propag. Lett.*, vol. 10, pp. 326–329, 2011.

[33] S. Zhu, H. Liu, P. Wen, L. Du, and J. Zhou, "A miniaturized and high gain double-slot Vivaldi antenna using wideband index-near-zero metasurface," *IEEE Access*, vol. 6, pp. 72015–72024, 2018.

[34] X. Shi, Y. Cao, Y. Hu, X. Luo, H. Yang, and L. H. Ye, "A high-gain antipodal Vivaldi antenna with director and metamaterial at 1–28 GHz," *IEEE Antennas Wireless Propag. Lett.*, vol. 20, pp. 2432–2436, 2021.

[35] X. Li, H. Zhou, Z. Gao, H. Wang, and G. Lv, "Metamaterial slabs covered UWB antipodal Vivaldi antenna," *IEEE Antennas Wireless Propag. Lett.*, vol. 16, pp. 2943–2946, 2017.

[36] S. Chamaani, S. A. Mirtaheri, and M. S. Abrishamian, "Improvement of time and frequency domain performance of antipodal Vivaldi antenna using multi-objective particle swarm optimization," *IEEE Trans. Antennas Propag.*, vol. 59, no. 5, pp. 1738–1742, May 2011.

[37] S. Chamaani, M. S. Abrishamian, and S. A. Mirtaheri, "Time-domain design of UWB Vivaldi antenna array using multiobjective particle swarm optimization," *IEEE Antennas Wireless Propag. Lett.*, vol. 9, pp. 666–669, 2010.

[38] H. Clavin, S. Das, and S. K. Sharma, "Design of a high gain broadband balanced antipodal Vivaldi antenna with 3D dielectric lens," in *Proc. IEEE Int. Symp. Antennas Propag. USNC-URSI Radio Sci. Meeting (AP-S/URSI)*, Denver, CO, USA, Jul. 2022, pp. 717–718.

[39] M. U. Afzal, K. P. Esselle, and B. A. Zeb, "Dielectric phase-correcting structures for electromagnetic band gap resonator antennas," *IEEE Trans. Antennas Propag.*, vol. 63, no. 8, pp. 3390–3399, Aug. 2015.

[40] P. Xie, G. Wang, X. Zou, and B. Zong, "Gain and AR improvements of the wideband circularly polarized Fabry–Pérot resonator antenna," *IEEE Trans. Antennas Propag.*, vol. 69, no. 10, pp. 6965–6970, Oct. 2021.

[41] M. U. Afzal, K. P. Esselle, and A. Lalbakhsh, "A methodology to design a low-profile composite-dielectric phase-correcting structure," *IEEE Antennas Wireless Propag. Lett.*, vol. 17, pp. 1223–1227, 2018.

[42] *New Material Innovations Guide for 3D Printing High Performance RF Components*, Rogers Corporation, Chandler, AZ, USA, 2021.

SANGHAMITRO DAS (Member, IEEE) received the B.Sc. degree (Hons.) in physics and the B.Tech. and M.Tech. degrees in radio physics and electronics from the University of Calcutta, Kolkata, West Bengal, India, in 2008, 2011, and 2013, respectively, and the Ph.D. degree in electromagnetics and microwaves from the Department of Electrical and Computer Engineering, University of Alberta, Edmonton, AB, Canada, in 2019.

He is currently a Postdoctoral Fellow with San Diego State University, San Diego, CA, USA. His current research interests include phased arrays for defense/space applications, novel electrically small antennas, high-gain and wideband antennas, 3-D-printable antenna systems, and metamaterial flat lenses.

Dr. Das received the Alberta Innovates Graduate Student Scholarship, in 2014, and the IEEE AP-S Doctoral Research Grant, in 2016, while pursuing the Ph.D. degree. He served as an Active Volunteer for the IEEE AP-S/MTT-S joint chapters of both Kolkata Section (Region 10) and Northern Canada Section (Region 7). He serves as a Reviewer for several IEEE journals, including IEEE TRANSACTIONS ON ANTENNAS AND PROPAGATION, IEEE TRANSACTIONS ON VEHICULAR TECHNOLOGY, IEEE ANTENNAS AND WIRELESS PROPAGATION LETTERS, IEEE ACCESS, IEEE OPEN JOURNAL OF ANTENNAS AND PROPAGATION, and IEEE OPEN JOURNAL OF THE COMMUNICATION SOCIETY.

HELENA CLAVIN received the B.S. degree in electrical engineering from San Diego State University, San Diego, CA, USA, in 2021.

She has been an Antenna Integration Engineer with the Embedded Solutions Team, Galtronics USA Inc., Tempe, AZ, USA, since 2022. The scope of her work ranges from performing active RF measurements to automating post-processing methods.

KAUSHIK DEBBARMA (Member, IEEE) received the Bachelor of Engineering degree in electronics and telecommunication engineering from the University of Pune, in 2011, the Master of Technology degree in communication engineering from NIT Agartala, in 2014, and the Ph.D. degree from the Department of Electronics and Electrical Engineering, IIT Guwahati, India, in 2021. He is currently a Postdoctoral Fellow with the Antenna and Microwave Laboratory, San Diego State University, San Diego, USA. His research interests include reflector antenna and feed systems, microstrip patch antenna, passive beam-steering antennas, Risley prisms, leaky wave antennas, and reconfigurable antennas.

SATISH KUMAR SHARMA (Senior Member, IEEE) received the B.Tech. degree in electronics engineering from the Kamla Nehru Institute of Technology, in 1991, and the Ph.D. degree in electronics engineering from the Indian Institute of Technology, Banaras Hindu University, in 1997. From March 1999 to April 2001, he was a Postdoctoral Fellow with the Department of Electrical and Computer Engineering, University of Manitoba, Winnipeg, MB, Canada. He was a Senior Antenna Engineer with InfoMagnetics Technologies Corporation, Winnipeg, from May 2001 to August 2006. Simultaneously, he was also a Research Associate with the University of Manitoba, from June 2001 to August 2006.

In August 2006, he joined the Department of Electrical and Computer Engineering, San Diego State University, San Diego, as an Assistant Professor. Here, he has developed the Antenna Laboratory. He teaches courses in applied electromagnetics and advises the B.S., M.S., and Ph.D. students and postdoctoral fellows. Since 2014, he has been a Full Professor and the Director of the Antenna and Microwave Laboratory. He has authored/coauthored more than 300 research papers published in the referenced international journals and conferences. He has co-edited three volumes of *Handbook of Reflector Antennas and Feed Systems* [Volume 1: Theory and Design of Reflectors, Volume II: Feed Systems, and Volume III: Applications of Reflectors (Artech House, USA)]. His new co-edited/coauthored book is *Multifunctional Antennas and Arrays for Wireless Communication Systems* (IEEE Press/Wiley, USA). His research interests include millimeter wave antennas, beam steering antennas, massive MIMO antennas, 5G communication antennas, beamforming networks, antennas for IoT, miniaturized antennas, ultra-wideband, multiband and broadband antennas, reconfigurable and frequency agile antennas, feeds for reflector antennas, waveguide horns and polarizers, electrically small antennas, RFID antennas, active antennas, frequency selective surfaces, metasurfaces, and microwave passive components. He is a Full Member of the USNC/URSI and Commission B and a Senior Member of URSI. He received the IEEE AP-S Harold A. Wheeler Prize Paper Award, in 2015; the National Science Foundation's Prestigious Faculty Early Development (CAREER) Award, in 2009; and the Young Scientist Award of URSI Commission B, Field and Waves, during the URSI Triennial International Symposium on Electromagnetic Theory, Pisa, Italy, in 2004. He was recognized as the Outstanding Associate Editor (AE) for IEEE TRANSACTIONS ON ANTENNAS AND PROPAGATION, in July 2014. He was the chair/co-chair of several student paper contests at different conferences and symposia. He served on the Sub-Committee of the Education Committee for the IEEE Antennas and Propagation Society for the Organization of the Student Paper Contests. He is currently serving as the Chair and Technical Activities for the USNC/URSI Commission B. He served as an AE for IEEE TRANSACTIONS ON ANTENNAS AND PROPAGATION and IEEE ANTENNAS AND WIRELESS PROPAGATION LETTERS.

PHILIP M. LAMBERT received the master's degree in mechanical engineering from Virginia Polytechnic Institute and State University, Blacksburg, VA, USA, in 2014.

Since then, he has worked in customer-facing technical roles across industries ranging from consumer electronics to implantable medical devices. Then, he joined Fortify, Boston, MA, USA, in 2019, where he is currently the Director of applications engineering. Fortify is a vertically integrated RF device and component manufacturer that uses novel additive manufacturing hardware, materials, and software to enable ultra-low SWaP-C systems. With over a decade of professional 3D printing experience, he is always working toward the goal of helping businesses to adopt 3D printing as a true manufacturing resource.

COLBY O. HOBART received the B.S. and M.S. degrees in electrical engineering from Worcester Polytechnic Institute, Worcester, MA, USA, in 2004. He has held a number of roles in passive RF design engineering and RF PCB fabrication support over a 20 years career. Recent roles include Senior RF Applications Engineer for Fortify, Boston, MA, USA, developing an application space for 3D printed low-loss material sets with tunable effective dielectric constant. In June 2024, he moved to Amphenol Printed Circuits to help create a competitive RF product line at the PCB and PCBA company.

◦ ◦ ◦